Hydroxyl vacancies in single-walled aluminosilicate and aluminogermanate nanotubes

2009 J. Phys.: Condens. Matter 21 195301

(http://iopscience.iop.org/0953-8984/21/19/195301)

J. Phys.: Condens. Matter **21** (2009) 195301 (9pp) doi:10.1088/0953-8984/21/19/195301

Hydroxyl vacancies in single-walled aluminosilicate and aluminogermanate nanotubes

Gilberto Teobaldi[1], Nikolaos S Beglitis[2,3], Andrew J Fisher[2,3], Francesco Zerbetto[4] and Werner A Hofer[1]

[1] Surface Science Research Centre, Department of Chemistry, University of Liverpool, Liverpool L69 3BX, UK
[2] London Centre for Nanotechnology, 17–19 Gordon Street, London WC1H 0AK, UK
[3] Department of Physics and Astronomy, University College London, Gower Street, London WC1E 6BT, UK
[4] Dipartimento di Chimica 'G Ciamician', Università degli Studi di Bologna, via Selmi 2, 40126 Bologna, Italy

Received 9 December 2008
Published 7 April 2009
Online at stacks.iop.org/JPhysCM/21/195301

Abstract
We report a theoretical study of hydroxyl vacancies in aluminosilicate and aluminogermanate single-walled metal-oxide nanotubes. Defects are introduced on both sides of the tube walls and lead to occupied and empty states in the band gap which are highly localized both in energy and in real space. Different magnetization states are found depending on both the chemical composition and the specific side with respect to the tube cavity. The defect-induced perturbations to the pristine electronic structure are related to the electrostatic polarization across the tube walls and the ensuing change in Lewis acid–base reactivity. A general approach towards a quantitative evaluation of both the polarization across the tube walls and the tube excluded volume is also proposed and discussed on an electrostatic basis.

S Supplementary data are available from stacks.iop.org/JPhysCM/21/195301

(Some figures in this article are in colour only in the electronic version)

1. Introduction

Since the discovery of carbon nanotubes by Ijima in 1991 [1], the field of carbon-based and inorganic nanotube materials has grown considerably due to their potential applications in electronics, photonics, chemical separation, (photo)catalysis and biotechnology [2]. While carbon nanotubes and their inorganic counterparts such as BN, WS_2 and MoS_2 are routinely produced by electric-arc discharge, chemical vapour deposition or laser ablation [2], new low-temperature solution-phase chemistry routes have recently been proposed for semiconducting single-walled aluminosilicate (Al–Si) and aluminogermanate (Al–Ge) nanotubes (figure 1 and [3]). The reported extremely high experimental control in terms of dimensions and monodispersity of these nanostructures [3], together with the potentially huge range of tunable properties via chemical functionalization and substitutional doping [4], make both Al–Ge and Al–Si attractive candidates as large-storage chemical devices [3], artificial ion-channel systems [2, 5] and insulating coatings for conducting cores, which could make it possible to enforce one-dimensional anisotropic conductivity at the nanoscale [6]. Al–Si and Al–Ge nanotubes are structurally analogous to the naturally occurring hydrous-aluminosilicate imogolite [7]. Its walls consist of a single layer of octahedrally coordinated aluminium hydroxide (gibbsite) with tetrahedral silanol (Si–OH) groups attached at the inner side of the tube (figure 1). From a compositional point of view, the only difference between Al–Si and Al–Ge tubes is the substitution of silanol groups with germanol (Ge–OH) moieties. The resulting chemical formulae of the unit cells are $(Al_2SiO_7H_4)_N$ and $(Al_2GeO_7H_4)_N$ for Al–Si and Al–Ge tubes, respectively. N refers to the number of radially inequivalent aluminium atoms along the nanotube circumference, necessarily an even number for symmetry reasons [8]. Regardless of the specific route adopted for their synthesis, both Al–Si and Al–Ge tubes are achiral

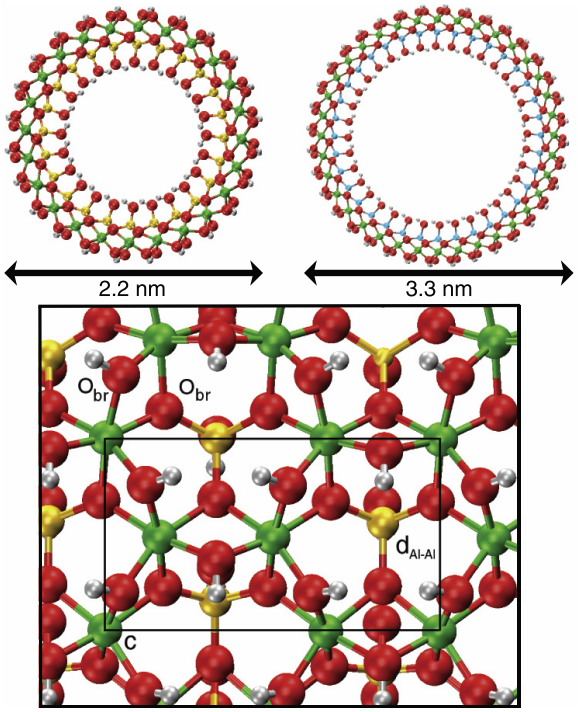

Figure 1. Optimized geometrical structure of $(Al_2SiO_7H_4)_{24}$ (left) and $(Al_2GeO_7H_4)_{36}$ (right) based nanotubes. The single-wall structural motif (bottom) is displayed together with the zig-zag periodic unit of size $\{c, d_{Al-Al}\}$ along the nanotube axis and circumference. Electronic version: O, red; H, grey; Al, green; Si, yellow; Ge, cyan.

and analogous to zig-zag $(n, 0)$ semiconducting carbon-based nanotubes [9]. Following a recent density functional theory (DFT) study of imogolite-based nanotubes [10], which opened up the possibility of first-principles studies for these systems, as well as previous simulations of neutral paramagnetic defects in zeolites [11], we address the effects of the simplest defects, i.e. neutral hydroxyl (–OH) vacancies[5], on Al–Ge and Al–Si in terms of both electronic structure changes and ensuing modifications in the global insulating properties.

2. Methods

DFT simulations were performed within an ultrasoft pseudopotential framework as currently implemented in the Vienna *ab initio* simulation package (VASP) [12]. On the basis of previous successful results for the same kind of systems as considered here [10], namely aluminosilicate mesostructures [13] and aluminium oxide thin films [14], exchange and correlation were approximated at the semi-local generalized gradient-corrected PW91-GGA level [15]. In all VASP simulations the adopted plane-wave energy cutoff was 400 eV. Geometrical scans were first carried out using the Γ point only and eventually the sampling of the irreducible Brillouin zone was performed with two special **k**-points. The results were found to be converged to within 0.01 eV/N, where N defines the number of aluminium atoms along the nanotube circumference in the repeat unit. The inter-tube separation enforced in the simulation was larger than 7.5 Å, which was checked to yield energies converged to within 0.002 eV/N with respect to a 14.5 Å distance among periodic replicates. Geometrical scans were first carried out adopting a 0.1 eV $Å^{-1}$ optimization threshold for all the nanotube atoms and eventually fully relaxing the nanotubes until the atomic forces were lower than 0.03 eV $Å^{-1}$. In all cases full atomic relaxations were performed according to a quasi-Newton approach and negligible differences were noted in the tube geometry between the first and last part of the optimization scheme. Geometrical optimization and electronic structure characterization of the corresponding bi-dimensional (2D) metal-oxide sheets were performed, enforcing a special **k**-point grid of $2 \times 3 \times 1$, both at PW91-GGA and hybrid B3LYP level. B3LYP [16] periodic calculations were carried with the Gaussian program [17] adopting a CEP-121G basis set [18][6]. Hydroxyl vacancy simulations were carried out within a spin-polarized approach. For diamagnetic results we checked that Gaussian smearing (σ = 0.01–0.05 eV, two **k**-points) and the tetrahedron method with Blöchl corrections (four **k**-points) yielded identical results. Defect formation energies were calculated as the energy difference between the OH_{vac} system on the one hand and the defect-free tube plus one neutral radical OH species (doublet state) on the other. Although these energies are overestimated due to the neglect of any solvent effects and the full hydration enforced in the simulation, the present results can be considered as a first approximation of the different energy penalties associated with the localization of the defect with respect to the nanotube cavity.

3. Result and discussion

3.1. Geometrical optimization

Due to the large computational requirements associated with the adopted first-principles approach, following [3, 19] we limited our investigations to $(Al_2SiO_7H_4)_{24}$ (N = 24) and $(Al_2GeO_7H_4)_{36}$ (N = 36) based nanotubes and their corresponding 2D-sheets. Both Al–Ge and Al–Si were originally built *in silico* assuming an undistorted octahedral (tetrahedral) coordination for Al (Si/Ge) atoms. In line with [8], we used Al–O and Si(Ge)–O bond lengths geometrically consistent with the optimized CLAYFF4 [20] nanotube radius of curvature (see [8] for the detailed procedure). The repeat unit size along the tube axis (c, figure 1) was scanned and the atomic position further optimized to evaluate the optimum repeat unit length which would eventually minimize the total nanotube energy. In order to reduce the computational cost to a bare minimum, the minimum step enforced during the scan was no smaller than

[5] Although it is generally recognized that the terminal hydroxyl (–OH) groups (both on the inner and outer surface) posses a net negative charge (see [8, 10]), the term neutral here refers to the global charge of the simulated system, i.e. the nanotube bearing one hydroxyl vacancy.

[6] Prior to B3LYP calculations, we checked the adopted CEP-121G electron core potential framework also at PW91 level. The calculated band gap (7.0 eV) was found to be in good agreement with previous PW91 results obtained with a double-zeta basis set with polarization functions (∼6.8 eV see [11]). On these grounds the CEP-121G basis set was also maintained at the B3LYP level.

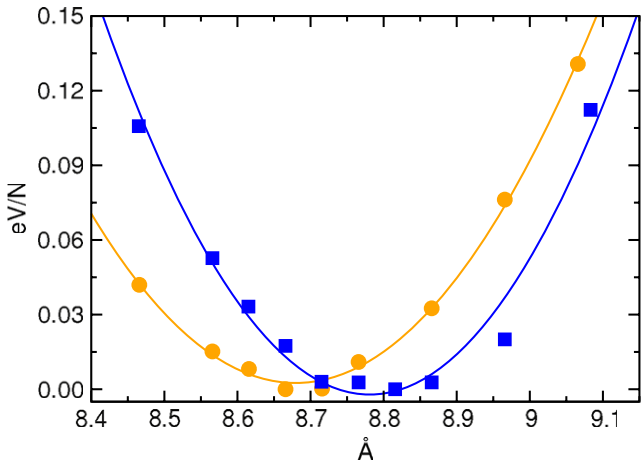

Figure 2. Total nanotube energy per number of Al atoms along the nanotube circumference (N) versus length of the repeat unit along the tube axis (c). Al–Ge tube, dark grey (electronic version: blue); Al–Si tube, light grey (electronic version: yellow).

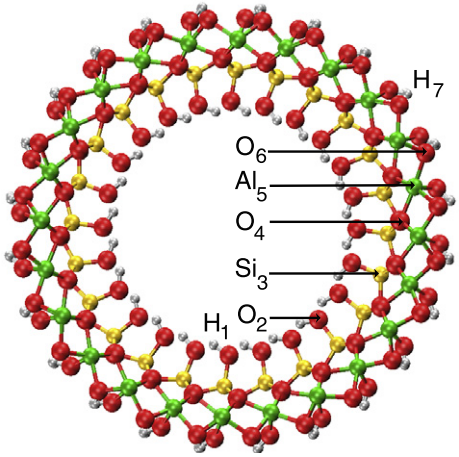

Figure 3. Radial atomic labelling for Al–Si (Al–Ge). Electronic version: O, red; H, grey; Al, green; Si, yellow.

0.05 Å. The optimum unit cell value was then successively evaluated on the basis of a least squares nonlinear fitting to the available data (figure 2). The calculated values are 8.68 ± 0.01 Å and 8.78 ± 0.01 Å for Al–Si and Al–Ge nanotubes, respectively. These results are slightly overestimated with respect to experimental x-ray diffraction (XRD) data for Al–Ge and Al–Si thin films, i.e. 8.51 Å [3]. Besides the known tendency of the adopted semi-local density functional approximation to overestimate aluminosilicate bond lengths [13, 21, 22], the deviations might also be due to interactions with crystallization solvent or among the nanotubes in the thin films—two aspects neglected here but which shall be the subject of future investigations. We also note that the agreement between the calculated value of 8.68 Å for $N = 24$, and 8.78 Å (8.72, 8.62 depending on the adopted basis set and **k**-point sampling) reported for $N = 20$ (equivalent to $N_u = 10$ in [10]) fully supports the assumption in [10] that the repeat unit cell size depends only weakly on the N parameter.

For comparison we also considered the analogous 2D-sheets of the Al–Ge and Al–Si systems. As for the nanotubes, the minimum energy shape and size of the zig-zag sheets were evaluated by changing both the size and angle of the unit cell first, and eventually fully optimizing the atomic coordinates within the enforced periodicity. The procedure revealed that a regular hexagonal arrangement of Al atoms is indeed also favoured for 2D-sheets. Concerning the optimum $\{c, d_{\mathrm{Al-Al}}\}$ sets, the calculations suggest {8.565, 4.945} Å and {8.652, 4.995} Å for Al–Si and Al–Ge 2D-sheets, respectively. The calculated minimum energy values for Al–Si sheets are in good agreement with recent double-zeta plus polarization basis set (DZP) results, i.e. {8.46, 4.9} Å [10]. Upon optimization of the bi-dimensional (2D) analogues of Al–Si and Al–Ge, the bending energy was evaluated to be -0.45 eV/N and -0.19 eV/N for Al–Si and Al–Ge tubes, respectively. These results confirm that the tube bending is a consequence of minimizing the strain from the mismatch between the stronger Si(Ge)–O and weaker Al–O bonds (see below and [3, 7]) in that the more bent Al–Si is more stabilized than Al–Ge by the bending process.

Adopting the same labelling as in [10] (figure 3), the calculated inner (outer) diameters for optimized Al–Si and Al–Ge are 12.33 ± 0.01 (23.15 ± 0.05) Å and 22.09 ± 0.03 (33.15 ± 0.04) Å. These values are in good agreement with the reported experimental (outer) value of ∼22 (∼33) Å for Al–Si (Al–Ge), and with recent results which have established a strong correlation between composition and diameter for imogolite-based nanotubes [23]. Table 1 reports the calculated diameters for the considered systems also in the presence of one OH_{vac}. With maximum deviation from the global averaged value of less than 0.07 Å, the calculated values strongly support the experimentally reported high monodispersity of both Al–Si and Al–Ge [3]. The radial distribution of the atomic layers (table 1 and figure 3), with O_2–Si_3 (O_4–Al_5) separations larger than Si_3–O_4 (Al_5–O_6) distances, is fully consistent with the reported structural data for imogolite crystals [7, 27]. Interestingly, it turns out that the radial distribution for Al–Ge tubes is different, in that while O_2–Ge_3 is still larger than Ge_3–O_4, upon optimization the O_4–Al_5 and Al_5–O_6 interlayer distances are modelled to be very close with a deviation of less than 0.1 Å. Despite the relatively large exothermic formation energies for Al–Si–OH_{invac} (+6.08 eV), Al–Si–OH_{outvac} (+6.32 eV), Al–Ge–OH_{invac} (+4.51 eV), Al–Ge–OH_{outvac} (+5.71 eV), we find that on a tube averaged basis the presence of OH_{vac} does not significantly alter the tube radii and monodispersity. In fact, the localized distortions due to removal of one hydroxyl group induce maximum deviations lower than 0.1 Å with respect to the averaged radial atomic distribution (table 1): deviations which are hardly detectable even by state of the art transmission electron microscopy (TEM) experiments like those reported in [3].

Upon inspection of the averaged bond lengths and angles for the optimized systems (table 2) the Al–O bond lengths are found to be in good agreement with previous GGA calculations on aluminosilicate clusters [13] and are practically not affected by the presence of either silanol or germanol groups in the tube cavity. The changes at Al–O level are also minimal

Table 1. Atomic radial distribution for Al–Si and Al–Ge optimized nanotubes. All diameters are reported in angstroms. The adopted labelling is reported in figure 3.

	Al–Si	Al–Si–OH_{invac}	Al–Si–OH_{outvac}	Al–Ge	Al–Ge–OH_{invac}	Al–Ge–OH_{outvac}
H_1	12.33 ± 0.01	12.32 ± 0.04	12.31 ± 0.08	22.09 ± 0.03	22.07 ± 0.05	22.06 ± 0.08
O_2	13.27 ± 0.02	13.27 ± 0.03	13.25 ± 0.08	22.94 ± 0.03	22.93 ± 0.02	22.88 ± 0.12
$Si_3(Ge_3)$	16.52 ± 0.02	16.52 ± 0.02	16.51 ± 0.09	26.43 ± 0.02	26.42 ± 0.09	26.38 ± 0.11
O_4	17.82 ± 0.07	17.81 ± 0.07	17.79 ± 0.10	27.78 ± 0.04	27.75 ± 0.06	27.73 ± 0.12
Al_5	19.75 ± 0.03	19.74 ± 0.04	19.71 ± 0.20	29.75 ± 0.02	29.73 ± 0.02	29.69 ± 0.20
O_6	21.91 ± 0.06	21.91 ± 0.06	21.89 ± 0.09	31.90 ± 0.04	31.89 ± 0.05	31.86 ± 0.09
H_7	23.15 ± 0.05	23.15 ± 0.05	23.15 ± 0.09	33.15 ± 0.04	33.14 ± 0.05	33.12 ± 0.12

Table 2. Structural parameters for Al–Si and Al–Ge optimized nanotubes. The data for the analogous 2D-sheets are reported within brackets.

	Al–Si	Al–Ge
Al–O (Å)	1.918 ± 0.052 (1.922 ± 0.072)	1.916 ± 0.054 (1.917 ± 0.057)
Si(Ge)–O (Å)	1.645 ± 0.005 (1.657 ± 0.028)	1.773 ± 0.013 (1.783 ± 0.023)
O–H (Å)	0.970 ± 0.010 (0.871 ± 0.009)	0.969 ± 0.011 (0.972 ± 0.008)
O_{br}–Al–O_{br} (deg)	78.6 ± 1.4 (82.9 ± 4.2)	78.0 ± 1.6 (81.7 ± 2.7)

with respect to values for the analogous 2D-sheet. The same also applies to O–H bond lengths. The main changes arising from the tube bending concern the Si(Ge)–O bonds, as indicated by the larger variations compared to the values of the corresponding 2D-sheets. With a shorter Si(Ge)–O bond length with respect to Al–O, the simulations confirm the bending process as a consequence of minimizing the structural strain originating from the stronger Si(Ge)–O bonds on the inner surface and the weaker Al–O bonds on the outer wall of the tubes. Finally, with a maximum deviation of ∼12° from an ideal octahedral (90°) coordination, the optimized bending angles indirectly support the assumption made in [8] that the Al–O coordination environment can be approximated by a rigid Al–O octahedron. However, it must be stressed that the present values have been calculated disregarding any solvent effects which may play a role. Although the presence of one OH_{vac} (both inside and outside the tube cavity) is calculated to marginally perturb the global tube monodispersity, on a local scale the defects induce different geometrical distortions depending on the specific metallic atom where OH_{vac} is created. In fact, while the Si(Ge)–O bonds increase from 1.645 (1.773) Å (table 2) to 1.662 (1.817) Å, one OH_{outvac} brings about a reduction of 0.027 Å and 0.052 Å for the Al–O bond opposite to the vacancy for Al–Si and Al–Ge, respectively. Again, the increased distortions for the Al–Ge tube can be considered as another indication of the higher thermodynamic stability of Al–Si with respect to Al–Ge. Concerning the changes on the bending angles induced by one OH_{vac}, the vacancies are calculated to cause a reduction of the O–Al–O angle inside the tube walls to 77.4° (77.2°) for Al–Si(Ge)–OH_{invac} and an increase to 80.8° (80.3°) for Al–Si(Ge)–OH_{outvac}.

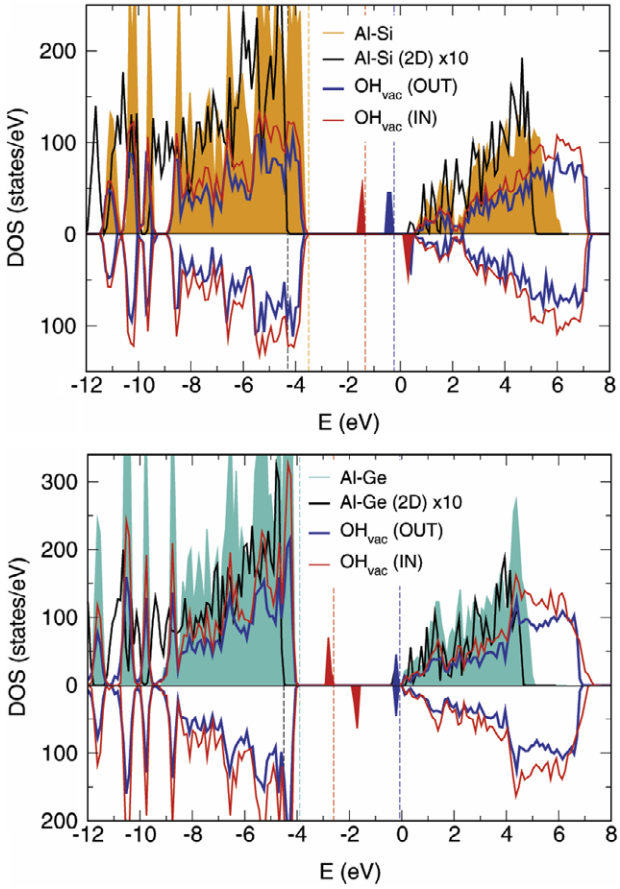

Figure 4. Total density of states (DOS) for defect-free Al–Si and Al–Ge, their 2D analogues, and in the presence of one OH_{vac} both on the outer (OUT) and the inner (IN) surface of the tubes. Calculated Fermi energies are displayed as a dotted line with the same colour labelling as for the DOS. 2D and band gap defect states (filled) have been increased by a factor of 10 for clarity.

3.2. Electronic structure

The calculated densities of states (DOS) for Al–Ge, Al–Si and the corresponding 2D-sheets are reported in figure 4. The calculated band gaps are 4.1 eV and 3.9 eV for Al–Si and Al–Ge, respectively. These values are also in accordance with simulations of aluminosilicate clusters (∼4 eV [13]) and aluminium oxide thin films (∼4 eV [14]) obtained using the same PW91 functional. We note that all these data match the

calculated band gaps recently reported for ($N = 20$) Al–Si, Al–Ge systems [10]. When considering the 2D-sheets, the physical bending of the nanotubes is found to affect only Al–Si but not Al–Ge. In fact, while we do not find any significant change in the calculated band gap between nanotube (3.9 eV) and 2D-sheet (4.0 eV) for the less warped Al–Ge tube, for the Al–Si tube, owing to the smaller radius of curvature, the calculated band gap is 0.4 eV smaller than for the corresponding 2D-sheet. For completeness we also considered the Al–Si (Al–Ge) 2D-sheets by adopting the hybrid functional B3LYP [16][7] which is reported to account correctly for the chemical reactivity of aluminosilicate-based materials [24]. In line with previous HF-based calculations for zeolites, which produced band gaps considerably larger than PW91 results [11], the B3LYP band gaps are wider than both the PW91 values and the experimental optical gap of 3.6 eV [3]. Specifically, within the triple-zeta basis set adopted, we found gaps of 9.3 eV and 7.42 eV for Al–Si and Al–Ge 2D-sheets, respectively. Bearing in mind the small influence of the tube bending on the modelled band gap, it is reasonable to expect that B3LYP will also overestimate the band gap for the complete nanotubes. On these grounds we expect the actual (indirect) band gap to be in the range 4.1–9.3 eV and 3.9–7.4 for Al–Si and Al–Ge tubes, respectively. This is in line with recent estimates based on (underestimated) GGA results as the lower limit, and (overestimated) density functional theory tight-binding (DFTB) values as the upper limit, for the actual band gap [19].

The experimental optical band gap of 3.6 eV [3] for Al–Ge is some way below the range between our (underestimated [14]) 3.9 eV PW91 value and the (overestimated [11]) 7.4 eV B3LYP result. This discrepancy supports previous suggestions [3] that strong excitonic effects may exist [25] in Al–Ge, as they do in carbon nanotubes [26].

Figure 5 shows the band-decomposed charge densities for both the valence band (VB) and conduction band (CB) edges, calculated by considering electronic states within 0.5 eV from the band onsets. Interestingly, it emerges that both Al–Si and Al–Ge are characterized by a neat separation in real space of the VB and CB. The VB edge is in fact localized inside the nanotube cavity, while the CB edge faces the outer side of the nanotube. We note that this kind of analysis also includes the interstitial charge density and consequently is free of the limitations which instead affect the corresponding atom resolved partial density of states (PDOS; see supporting information SI available at stacks.iop.org/JPhysCM/21/195301). For completeness we report that our PDOS analyses (carried out, we stress, on the basis of the charge density contained within the core-size radius of the atoms as in [10]) reveal a predominant oxygen contribution to both the high-energy valence band (VB) edge (2p character) and to the low-energy conduction band (CB) edge (2s–2p hybridized states) regardless of the presence of OH_{vac}. Although in line with [10, 19] concerning the VB edge, this analysis assigns the predominant component of the CB edge to O atoms and not to (outer) H_7 (figure 3) atoms as

[7] On the basis of relatively small bending effects on the modelled band gap of Al–Si and Al–Ge systems, and due to the increased computational cost, the hybrid functional analysis was carried out only for 2D-sheets.

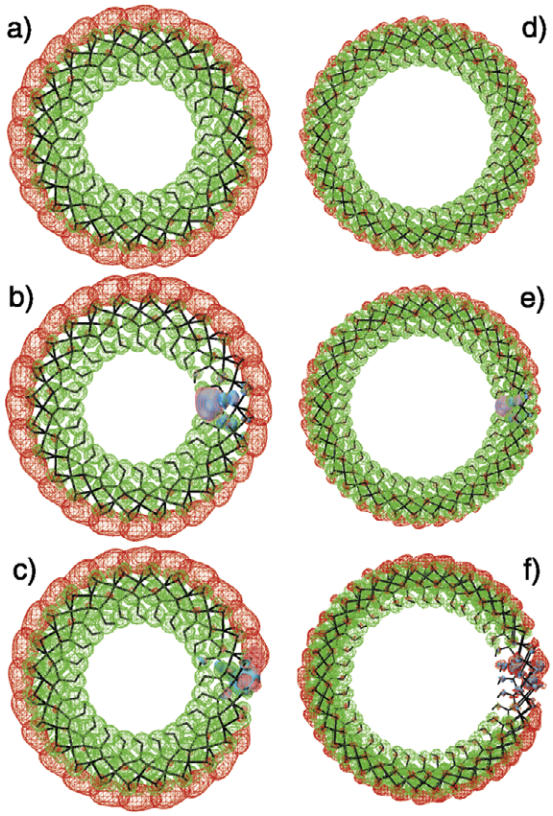

Figure 5. Band-decomposed charge density for defect-free Al–Si (a) and Al–Ge (d), and in the presence of one OH_{vac} both inside (b, e) and outside (c, f) the nanotube cavity. The VB (green in the electronic version, $10^{-6}e$ Å^{-3}) and CB (red in the electronic version, $5 \times 10^{-7}e$ Å^{-3}) densities have been integrated over 0.5 eV from the band onset. Occupied and empty band gap defect states are displayed ($5 \times 10^{-7}e$ Å^{-3}) in cyan and pink, respectively (electronic version).

in [10] or to 3p and 3d Si states and 3s Al states as suggested in [19]. In our view, this disagreement can be traced back to the quite small plane-wave energy cutoff (10 eV) for the atom-resolved PDOS analysis and to the minimal atomic basis set used in [10] and [19], respectively. Disregarding the partial disagreement concerning the main contributions to the CB edge, the modelled real space localization of both the VB and CB edges confirms a strong radial anisotropic electron affinity with an ensuing enhanced Lewis acidity (basicity) for the outer (inner) tube surfaces as suggested in [27] and backed up by simulations in [10, 19].

In order to investigate the effects of OH vacancies on the global electronic structure of the tube, one hydroxyl fragment was eliminated on either the inner, Al–Si(Ge)–OH_{invac}, or on the outer, Al–Si(Ge)–OH_{outvac}, side. In analogy with O vacancies on other metal-oxide substrates [28], the presence of one OH_{vac} is found to introduce electronic states in the pristine band gap (figure 4). One OH_{invac} is found to create both occupied and unoccupied defect states, which reduce the calculated band gap to ∼1.8 and ∼1.1 eV for both Al–Si and Al–Ge. Therefore, despite the defect-induced reduction of the band gap and the ensuing enhancement of the finite-temperature conductivity, we expect the considered systems

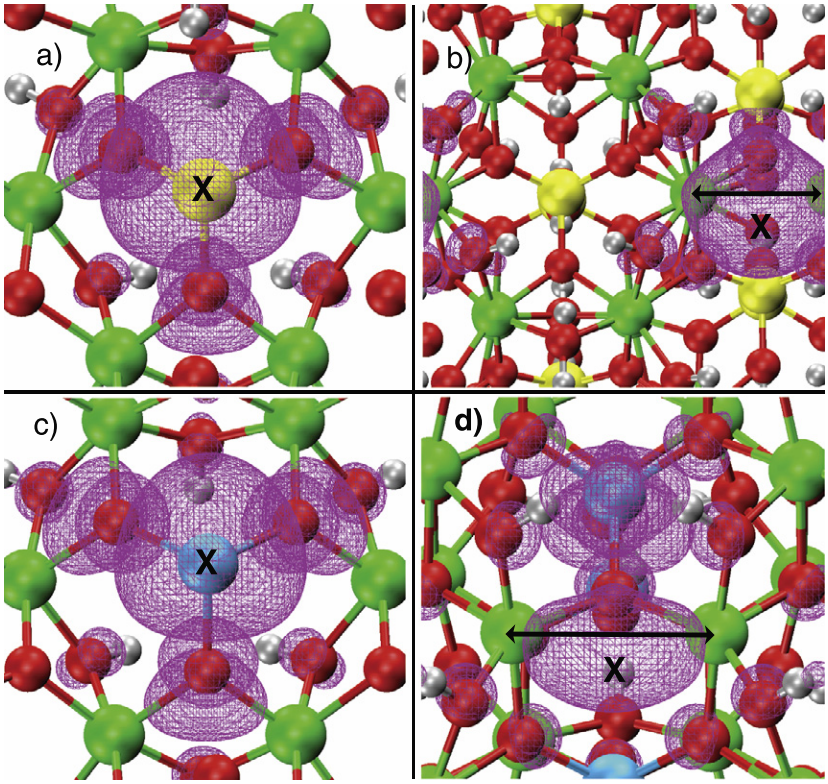

Figure 6. Close up of band-decomposed charge density ($5 \times 10^{-7} e$ Å^{-3}) for occupied defect states associated with OH_{vac} (X): (a) Al–Si–OH_{invac}; (b) Al–Si–OH_{outvac}; (c) Al–Ge–OH_{invac}; (d) Al–Ge–OH_{outvac}. OH_{invac} and OH_{outvac} are shown from inside and outside the tube cavity, respectively. Undercoordinated Al atoms for OH_{outvac} are highlighted by mean of arrows. Electronic version: O, red; H, grey; Al, green; Si, yellow; Ge, cyan.

to remain insulating at room temperature. Both defects are magnetic, generating a doublet spin-state. In line with previous results for paramagnetic defects in zeolites [11], the occupied (unoccupied) defect states for both for Al–Ge and Al–Si are highly localized around the undercoordinated Si (Ge) atom (figures 5, 6). Interestingly, while one OH_{vac} on the outer wall of Al–Si is also found to create a localized paramagnetic (doublet) spin-state (figures 5, 6) and to reduce the calculated band gap (0.8 eV), the same defect in the Al–Ge analogue forms a state just at the CB onset which pins the Fermi level there. Consequently, despite the odd total electron count in the system, our DFT energy is minimized by a non-magnetic solution with equal occupancy of both up and down spins (figure 4 and supporting information SI available at stacks.iop.org/JPhysCM/21/195301). In order to asses whether this behaviour would also be found for a truly isolated defect, or is an artefact of the periodic defect structure along the tube imposed by our boundary conditions, we considered one OH_{vac} on the outer topmost face of a 4 × 2 super cell of the 2D-Al–Ge sheet (see supporting information SI, available at stacks.iop.org/JPhysCM/21/195301). We note that while the shortest distance between defects in replicated cells is 8.78 Å for Al–Si(Ge)–OH_{outvac}, in the present case it is 17.3 Å. Interestingly, for the 4 × 2 2D-system, the presence of one OH_{vac} is also modelled to induce a non-magnetic solution. On this basis, and bearing in mind the small influence that tube bending has on the modelled band gap, we believe that the non-magnetic solution is indeed physically significant; the reduced band gap of Al–Ge with respect to Al–Si, which lowers the conduction band edge relative to the defect states, is suggested as the main cause of this metallization effect. To the best of our knowledge, the present contribution represents the first DFT study of vacancies in extended aluminogermanate structures.

3.3. Surface polarization

It has been suggested that the surface charge properties and chemical reactivity of imogolite depend on a delicate (pH-dependent) balance between local geometrical deformations associated with the tube bending and positive (negative) charge accumulation on the outer (inner) surface [27]. Charge separation across the tube walls is also expected to play a fundamental role for the suggested use of Al–Si (Al–Ge) as an insulating coating around conducting cores [3, 6]. In this respect, it is of utmost importance to assess the changes induced by OH_{vac} in terms of both local and global polarization across the tube section.

By using Gauss's theorem within a cylindrical condenser approximation [29] it is possible to relate the change ($\Delta\overline{V}$) in the (microscopically) averaged electrostatic potential across the polarized interface to the electrostatic dipole density across the interface itself (μ_σ) as:

$$\Delta\overline{V} = 4\pi\,\mu_\sigma \ln\left(\frac{R_{in}}{R_{out}}\right) \qquad (1)$$

Table 3. Averaged electrostatic potential $\overline{V}$ changes (eV) for O_4/O_6 layers with respect to O_2. Angular sectors of $\pm 15°$ ($2\pi/24$) and $\pm 10°$ ($2\pi/36$) around the defect sites have been averaged for Al–Si–OH_{vac} and Al–Ge–OH_{vac}, respectively (see equation (2)).

	Al–Si	Al–Si–OH_{invac}	Al–Si–OH_{outvac}	Al–Ge	Al–Ge–OH_{invac}	Al–Ge–OH_{outvac}
O_2	0	0	0	0	0	0
O_4	−9.8	−11.2	−11.0	−10.6	−10.7	−13.1
O_6	−5.4	−5.5	−5.3	−6.0	−6.4	−1.7

where atomic units are used, R_{in} (R_{out}) defines the inner (outer) radius of the tube and the microscopically averaged potential $\overline{V}$ in cylindrical coordinates ($r = \sqrt{x^2 + y^2 + z^2}, x = r\cos\phi, y = r\sin\phi, z$) reads:

$$\overline{V}(r) = \frac{1}{2\pi c_0} \int \int V(r, \phi, z)\, \mathrm{d}z\, \mathrm{d}\phi \qquad (2)$$

where c_0 defines the optimized length of the simulation cell along the tube axis z (figure 1).

On this basis, it is straightforward to evaluate the actual dipole density across the tube walls from the $\Delta\overline{V}$ values calculated by DFT simulations. Besides providing the electrostatic potential (V), DFT simulations can also be conveniently used to infer a value for R_{in} (R_{out}) which accounts not only for atomic positions but also for the electronic distribution of the nanotube itself. In fact, from the onset of the electrostatic plateaus characterizing the vacuum region (figure 7), it is possible to also define the spatial extent of the total charge distribution of the tube. Alternatively, one could define R_{in} (R_{out}) on the basis of the real space positions for which the microscopically averaged (global) charge density ($\overline{\rho}$) becomes zero within the convergence tolerance enforced in the DFT simulation itself. Since the electrostatic potential and the (global) charge density are related by Poisson's equation [$\nabla^2\overline{V}(x, y, z) = -4\pi\overline{\rho}(x, y, z)$], the two approaches necessarily yield equivalent results as shown in figure 7. We note that according to this procedure the calculated polarization across the tube walls accounts for the total distribution of the tube charge density and as such also the contribution from interstitial charge and local gradients contributes to the final net polarization. Additionally, the (converged) plane-wave approach yields results independent of the basis set, at odds with Mulliken based analysis [10, 19]. In the present application we relied on the electrostatic potential, V as given by the VASP program [12] and calculate the global charge density ρ by fast Fourier transform (FFT) expansion of the Poisson equation in reciprocal space[8]. From the change in the averaged electrostatic potential, Al–Ge ($R_{in} = 8.7$ Å, $R_{out} = 18.2$ Å) is calculated to possess a dipole density across the wall (0.06 debye $Å^{-2}$), which is twice the value for Al–Si (0.03 debye $Å^{-2}$, $R_{in} = 4.2$ Å, $R_{out} = 13.7$ Å). Thus, in line with [27] and [19] (but at odds with [10]), the calculated

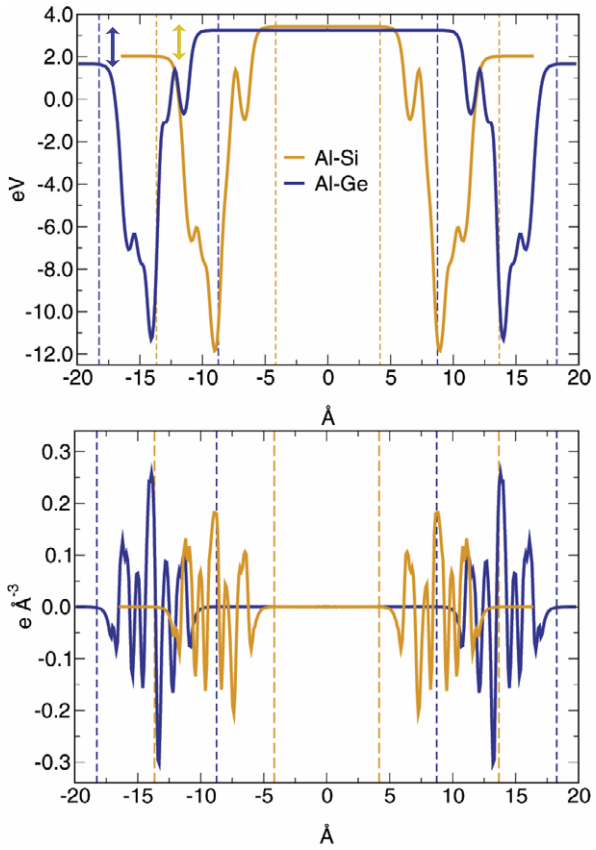

Figure 7. Top: radial distribution of the averaged electrostatic potential $\overline{V}$. Vertical arrows highlight the electrostatic potential shifts $\Delta\overline{V}$ across the tube walls. Bottom: radial distribution of the averaged global charge density $\overline{\rho}$. The vertical dotted lines define the radial extent of the tube walls as emerging from the calculated $\overline{V}$ or $\overline{\rho}$ plateaus (see the text for details).

polarization directions agree with positive (negative) charge accumulation at the outer (inner) surface as suggested by the higher inner $\overline{V}$ plateau with respect to the outer value for both Al–Si and Al–Ge (figure 7).

With the aim of providing deeper insight into the chemical differences which characterize the outer and inner surfaces of Al–Si and Al–Ge, we considered the change in electrostatic potential associated with specific atomic layers (see figures 3, 7 and tables 1, 3). This kind of analysis is convenient because its results can be directly related to the relative increase/decrease of local Lewis acid–base reactivity for the considered site within each simulation cell. The lower the electrostatic potential, the higher the acidity, i.e. the electron acceptor affinity for the considered site. Table 3 reports an O atom resolved analysis of the electrostatic potential acting

[8] We evaluated ρ calculating first the FFT coefficients $\hat{V}_G$ of the electrostatic potential with the same grid ($G = 0, 1, 2, \ldots G_{max}$) enforced in the corresponding VASP simulations, and eventually obtaining the FFT coefficients of the charge density as $\hat{\rho}_0 = 0$, $\hat{\rho}_G = \frac{G^2}{4\pi}\hat{V}_G$, where G defines the length of the reciprocal lattice vectors used in the FFT expansion. Finally, ρ was obtained by back transformation of $\hat{\rho}_G$, see [30, p. 89] for details. FFT evaluations were performed via the open source (complex double precision) netlib FFT-pack [31].

at $O_2/O_4/O_6$ level for all the systems considered. While a direct comparison among $O_2/O_4/O_6$ sites of a given system is physical meaningful, on the basis of both the electrostatic averaging procedure enforced in our DFT simulations [30] and the different charge distribution for each simulation cell, no comparison should be attempted between different systems (i.e. different columns of table 3) in the absence of any electrostatic alignment procedure (here neglected). Disregarding the tube composition and defect presence, the inner O_2 layer is evaluated to be a weaker Lewis acid (i.e. electron acceptor) than the outer O_6 layer as expected on the basis of the experimental [27] and calculated charge distribution across the tube walls (figure 7 and [19]). The simulations also suggest the O_4 layer as the most acidic site. Due to defect-induced charge reorganization, the presence of one OH_{vac} is modelled to alter locally the acid–base properties of the O layers. Specifically, the relative Lewis acidity of O_4/O_6 layers with respect to O_2 increases upon formation of one OH_{invac} owing to the highly localized Al–Si(Ge)–OH_{invac} states (figures 5, 6). Conversely, and not surprisingly, the relative acidity of O_4 with respect to O_2 is reduced when one OH_{outvac} is created on the surface. As a final remark we stress that, while convenient in terms of relative Lewis acid–base reactivity, the present analysis for $O_2/O_4/O_6$ layers cannot provide quantitative insights into the global polarization across the nanotube walls. To this end, the global charge organization across the wall, i.e. the inner and outer electrostatic plateaus (figure 7), must be accounted for and no dipole evaluation should be attempted on the basis of the reduced set of data displayed in table 3.

3.4. Mechanical properties: linear Young's modulus

In view of their possible use as (insulating) coatings for one-dimensional nanodevices [3, 6], the elastic properties of imogolite-based nanotubes with respect to external mechanical perturbations also need to be addressed. To the best of our knowledge, this aspect has so far only been investigated at the DFT-TB level [19] and no first-principles (or experimental) results are currently available.

The geometric optimization protocol we followed already provides the required information to calculate the simplest mechanical property associated with the nanotubes, namely their Young's modulus (Y). In fact, given the axial tensile ($\epsilon > 0$) or compressive ($\epsilon < 0$) strain defined as:

$$\epsilon = \frac{c - c_0}{c_0}, \tag{3}$$

where c_0 is the optimized length of the simulation cell along the tube axis z (figure 1), the Young's modulus (Y) can be obtained on the basis of the computed energies (E) as a function of the tube (simulation cell) length c (figure 2) as [32, 33]:

$$Y = \frac{1}{V_0}\left(\frac{\partial^2 E}{\partial \epsilon^2}\right)_{\epsilon=0}, \tag{4}$$

where V_0 is the optimized tube volume for a simulation cell of length c_0. Apart from the computational accuracy of $E(\epsilon)$, a critical issue in equation (4) is the definition of the equilibrium volume V_0. From elementary geometry, for a hollow cylinder it follows that $V_0 = 2\pi\, R_{in}\, \Delta R\, c_0$, where R_{in} is the inner radius, ΔR the thickness of the tube wall and c_0 as defined above. It readily emerges that different choices of R_{in} and ΔR affect the final value of the calculated Young's modulus (Y). Since by definition $\Delta R = R_{out} - R_{in}$, it is also possible in this case to rely on the result for the electrostatic potential (or global charge density) analysis (figure 7) in order to define values for R_{in} (R_{out}) which account for the electronic distribution of the nanotube, thus providing a value for V_0, which is representative of the *excluded volume* at the equilibrium geometry. The calculated values for Al–Si and Al–Ge tubes are reported in table 4 for different choices of R_{in}, R_{out} determined both on the basis of the modelled $\overline{V}$ plateaus (see figure 7 and equations (2)) and optimized (H_1, H_7), (O_2, O_6) radii (see figure 2 and table 1). In line with previous DFT-TB suggestions [19], with calculated values in the range 100–200 GPa, the modelled stiffness for imogolite-based system is comparable with GaAs ($\sim$ 270 GPa) and MoS_2 ($\sim$230 GPa) nanotubes but smaller than for other $C_xB_yN_z$ tubes [32–34]. Because the GGA framework we adopt is known to underestimate the elastic constants of extended metal-oxide structures [35], we expect our results to be a lower limit for the experimental Young's moduli for both Al–Si and Al–Ge tubes which, to the best of our knowledge, have not yet been experimentally determined.

Table 4. Calculated Young's moduli (GPa) for defect-free Al–Si and Al–Ge nanotubes. The adopted values for (R_{in}, ΔR) (Å) are shown within brackets (see text for details).

	Al–Si	Al–Ge
$\overline{V}$, $\overline{\rho}$	122 ± 2 (4.2, 9.5)	102 ± 4 (8.7, 9.5)
H_1, H_2	144 ± 3 (6.2, 5.4)	146 ± 7 (11.1, 5.5)
O_2, O_6	168 ± 3 (6.6, 4.3)	174 ± 8 (11.5, 4.5)

4. Summary

The presence of hydroxyl vacancies has been modelled for $(Al_2SiO_7H_4)_{24}$ and $(Al_2GeO_7H_4)_{36}$ single-walled metal-oxide nanotubes. With the exception of one OH_{vac} localized on the outer wall of the $(Al_2GeO_7H_4)_{36}$ tube, the defects are found to induce occupied and empty states in the band gap which are highly localized both in energy and in real space. A general approach aimed at a quantitative evaluation of both the polarization across the tube walls and the tube excluded volume has been proposed and discussed in comparison with other previous conventions. In line with previous experimental suggestions, the calculated polarization directions confirm positive (negative) charge accumulation at the outer (inner) surface of the nanotubes.

Acknowledgments

We gratefully acknowledge support from the Engineering and Physical Sciences Research Council (EPSRC, UK, EP/C541898/1 and EP/C54188X/1) and the Royal Society (WAH). GT thanks Daniel Sanchez-Portal and Nicolas Lorente for useful discussions.

References

[1] Iijima S 1991 *Nature* **10** 56
[2] Baughman R H 2000 *Science* **290** 1310
Dresselhaus M S and Dai H 2004 *MRS Bull.* **29** 237
Remskar M 2004 *Adv. Mater.* **16** 1497
Tenne R and Rao C N R 2004 *Phil. Trans. R. Soc.* A **362** 2099
Bianco A, Kostarelos K and Prato M 2005 *Curr. Opin. Chem. Biol.* **9** 674
[3] Mukherjee S, Bartlow V M and Nair S 2005 *Chem. Mater.* **17** 4900
Mukherjee S, Kim K and Nair S 2007 *J. Am. Chem. Soc.* **129** 6820
[4] Han W Q, Wen W, Yi D, Liu Z, Maye M M, Lewis L, Hanson J and Gang O 2007 *J. Phys. Chem.* C **111** 14339
[5] Konduri S K, Tong H M, Chempath S and Nair S 2008 *J. Phys. Chem.* C **112** 15367
[6] Edwards P P, Anderson P A, Woodall L J, Porch A and Armstrong A R 1996 *Mater. Sci. Eng.* A **217/218** 198
[7] Cradwick P D, Wada K, Russell J D, Yoshinaga N, Masson C R and Farmer V C 1972 *Nature (Phys. Sci.)* **240** 187
Bursill L A, Peng J L and Bourgeois L N 2000 *Phil. Mag.* A **80** 105
[8] Konduri S, Mukherjee S and Nair S 2006 *Phys. Rev.* B **74** 033401
[9] Saito R, Dresslhaus G and Dresselhaus M S 1998 *Physical Properties of Carbon Nanotubes* (London: Imperial College Press)
[10] Alvarez-Ramírez F 2007 *Phys. Rev.* B **76** 125421
[11] Catlow C R A, Cora F and Sokol A A 2000 *Comput. Mater. Sci.* **17** 312
[12] Kresse G and Hafner J 1993 *Phys. Rev.* B **47** 558
Kresse G and Furthmüller J 1996 *Phys. Rev.* B **54** 11169
[13] Li H, Mahanti S D and Pinnavaia T J 2005 *J. Phys. Chem.* B **109** 2679
[14] Kresse G, Schmid M, Napetschnig E, Shishkin M, Khler L and Varga P 2005 *Science* **308** 1440
[15] Perdew J P, Chevary J A, Vosko S H, Jackson K A, Pederson M R, Singh D J and Fiolhais C 1992 *Phys. Rev.* B **46** 6671
[16] Becke A D 1993 *J. Chem. Phys.* **98** 5648
[17] Frisch M J, Trucks G W, Schlegel H B, Scuseria G E, Robb M A, Cheeseman J R, Montgomery J A Jr, Vreven T, Kudin K N, Burant J C, Millam J M, Iyengar S S, Tomasi J, Barone V, Mennucci B, Cossi M, Scalmani G, Rega N, Petersson G A, Nakatsuji H, Hada M, Ehara M, Toyota K, Fukuda R, Hasegawa J, Ishida M, Nakajima T, Honda Y, Kitao O, Nakai H, Klene M, Li X, Knox J E, Hratchian H P, Cross J B, Bakken V, Adamo C, Jaramillo J, Gomperts R, Stratmann R E, Yazyev O, Austin A J, Cammi R, Pomelli C, Ochterski J W, Ayala P Y, Morokuma K, Voth G A, Salvador P, Dannenberg J J, Zakrzewski V G, Dapprich S, Daniels A D, Strain M C, Farkas O, Malick D K, Rabuck A D, Raghavachari K, Foresman J B, Ortiz J V, Cui Q, Baboul A G, Clifford S, Cioslowski J, Stefanov B B, Liu G, Liashenko A, Piskorz P, Komaromi I, Martin R L, Fox D J, Keith T, Al-Laham M A, Peng C Y, Nanayakkara A, Challacombe M, Gill P M W, Johnson B, Chen W, Wong M W, Gonzalez C and Pople J A 2004 *Gaussian 03, Revision C.02* (Wallingford, CT: Gaussian)
[18] Cundari T R and Stevens W J 1993 *J. Chem. Phys.* **98** 5555
[19] Guimarães L, Enyashin A N, Frenzel J, Heine T, Duarte H A and Seifert G 2007 *ACS Nano* **1** 362
[20] Cygan R T, Liang J J and Kalinichev A G 2004 *J. Phys. Chem.* B **108** 1255
[21] Gale J D, Rohl A L, Milman V and Warren M C 2001 *J. Phys. Chem.* B **105** 10236
[22] Refson K, Park S H and Sposito G 2003 *J. Phys. Chem.* B **107** 13376
[23] Konduri S, Mukherjee S and Nair S 2007 *ACS Nano* **1** 393
[24] Hemelsoet K, Lesthaeghe D, Van Speybroeck V and Waroquier M 2007 *J. Phys. Chem.* C **111** 3028
[25] Scholes G D 2008 *ACS Nano* **2** 523
[26] Wang F, Cho D J, Kessler B, Deslippe J, Schuck P J, Louie S G, Zettl A, Heinz T F and Shen Y R 2007 *Phys. Rev. Lett.* **99** 227401
[27] Gustafsson J P 2001 *Clays Clay Miner.* **49** 73
[28] Henrich V E and Cox P A 1996 *The Surface Science of Metal Oxides* (Cambridge: Cambridge University Press)
[29] Tipler P A and Mosca G P 2007 *Physics for Scientists and Engineers* 6th edn (New York: Freeman)
[30] Kantorovich L 2004 *Quantum Theory of the Solid State: an Introduction* (London: Kluwer Academic)
[31] Swarztrauber P N 1982 *Vectorizing the FFTs, in Parallel Computations* ed G Rodrigue (New York: Academic) pp 51–83 http://www.netlib.org/fftpack/
[32] Lu J P 1997 *Phys. Rev. Lett.* **79** 1297
[33] Hernández E, Goze C, Bernier P and Rubio A 1998 *Phys. Rev. Lett.* **80** 4502
[34] Hernández E, Goze C, Bernier P and Rubio A 1999 *Appl. Phys.* A **68** 287
[35] Ravindran P, Vidya R, Vajeeston P, Kjekshus A and Fjellvag H 2003 *J. Solid State Chem.* **176** 338